PHYSICAL REVIEW A VOLUME 56, NUMBER 1 JULY 1997

Molecules in intense laser fields: Enhanced ionization in one- and two-electron linear triatomic molecules

Hengtai Yu and André D. Bandrauk
Laboratoire de Chimie Théorique, Faculté des Sciences, Université de Sherbrooke, Sherbrooke, Québec, J1K 2R1 Canada

(Received 19 December 1996)

Numerical solutions of the time-dependent Schrödinger equation are presented to study the behavior of one and two electrons in symmetric and nonsymmetric linear molecules $H_3{}^{2+}$ and $H_3{}^{+}$. Enhanced ionization, as discovered earlier in diatomic molecules $H_2{}^{+}$ and H_2 are shown to occur also in triatomic systems at critical internuclear separations that are determined by both field-induced barrier localization of the electron and charge resonance (CR) transitions. Two-electron effects manifest themselves through their influence on CR transition moments and electron collisions at large intensities. [S1050-2947(97)02407-4]

PACS number(s): 42.50.Hz

I. INTRODUCTION

The interaction of intense laser fields with atoms has lead to many unexpected nonlinear multiphoton optical phenomena of a nonperturbative nature such as above-threshold ionization (ATI) and laser-induced stabilization [1]. Molecules are being investigated currently in similar fashion as they offer the possibility of more complex behavior due to the additional degrees of freedom arising from the nuclear motion. Thus the analog of ATI for nuclear motion, above thresheld dissociation (ATD), is now well documented in terms of a dressed state representation of field-electronic molecular surfaces on which nuclei propagate [2–4].

Electronic ionization and the Coulomb explosion of molecules have only recently been addressed experimentally and theoretically [4–27]. A fundamental difference between atoms and molecules has been the prediction of the phenomenon of charge resonance enhanced ionization (CREI) from numerical similations [11–22] and its recent experimental confirmation [8–10,23]. Both laser-induced barrier tunneling models [5–7,12,20,21] and laser-induced charge localization models [11,13,18] show that such enhanced ionization rates occur in diatomic molecules in the presence of intense laser fields at large critical internuclear distances, exceeding the rates of the dissociation fragments by one or two orders of magnitude. The kinetic energies of the Coulomb explosion fragments are hence predicted and found experimentally to be much less than those obtained from direct Franck-Condon ionizations from the initial ground state as these explosions occur at the large critical distances mentioned above [5–10,22]. Exact numerical simulations of Coulomb explosions in $H_2{}^{+}$ confirm the theoretical predictions and the experimental observation of low-kinetic-energy fragments [15,16] as due to CREI at large distances. We address in the present paper the laser-enhanced ionization phenomenon in linear triatomic molecules such as the one-electron $H_3{}^{2+}$ and the two-electron $H_3{}^{+}$ molecules for both symmetric and nonsymmetric dissociation. Previous three-dimensional (3D) simulations on this one-electron triatomic system have found that the field induced over the barrier ionization models can explain qualitatively CREI and its phase control in such system [18], whereas 1D simulations have shown that field barrier effects dominate ionization of highly charged one-electron triatomic molecules [21]. As in our previous simulations in H_2 [17], we shall compare one- and two-electron systems in a linear triatomic array of three protons. The spectroscopy of the two-electron system $H_3{}^{+}$ is now well documented [28]. The ground state is found to be triangular and the linear geometry exists at 1.77 eV above the ground state. We shall explore nonlinear effects for the linear geometry as an attempt to understand one- and two-electron effects in extended systems in intense laser field. We have already shown previously that the one-electron linear $H_3{}^{2+}$ can be stabilized at high intensities and frequencies due to high nonlinear electron-field interactions [29]. We shall examine in the present paper the nonlinear electronic properties of this system in the region of current experimental conditions, $I \simeq 10^{14}$ W/cm^2 and $\lambda =$ 1064 nm, by solving the appropriate time-dependent Schrödinger equation (TDSE).

II. NUMERICAL METHOD

The main numerical method for solving the TDSE have been given in our previous paper on the 3D $H_3{}^{2+}$ [18] and 1D H_2 [17]. For the 1D, three-proton, two-electron problem we write

$$i\frac{\partial}{\partial t}\Psi(x_1,x_2,t)=[H_k(x_1,x_2,t) + V_{ext}(x_1,x_2,t)]\Psi(x_1,x_2,t), \qquad (1)$$

where $H_k = T + V_c$ and

$$\begin{aligned} V_c = & -\left[1+\left(x_1-\frac{R}{2}\right)^2\right]^{-1/2} - \left[1+\left(x_1+\frac{R}{2}\right)^2\right]^{-1/2} \\ & -\left[1+\left(x_2-\frac{R}{2}\right)^2\right]^{-1/2} - \left[1+\left(x_2+\frac{R}{2}\right)^2\right]^{-1/2} \\ & -[1+(x_1)^2]^{-1/2} - [1+(x_2)^2]^{-1/2} \\ & +[1+(x_1-x_2)^2]^{-1/2}, \end{aligned} \qquad (2)$$

$$V_{\text{ext}} = (x_1+x_2)E(t),$$

where T is the kinetic-energy operator, x_1 and x_2 are the coordinates of the two electrons, and R is the internuclear distance between the two outer hydrogen atoms in the symmetric $H_3{}^+$ case. In the nonsymmetric case that we label as $H_3{}^{2+}(n)$ and $H_3{}^+(n)$, and R is the distance between the external proton and the adjacent proton in $H_2{}^+$ or H_2, which are fixed at $R_e=2.0$ a.u.

In this work, the nuclei of the triatomic molecule are considered as fixed, with the bond oriented along the x axis. The size of the grid used for the numerical calculations is taken to be 256 a.u. with 1024 grid points in both x_1 and x_2 coordidates. The linearly polarized external laser field $E_0(t)$ is set parallel to the x axis, with a five-cycle ramp time, after which it is kept constant during the simulation.

An absorbing potential along each x_1 and x_2 electron direction is used during all propagation to prevent reflection of wave functions at the box edge. This absorbing potential V_{abs} is of the form $V_{abs}(x)=\cos\{[(x-x_1)/x_a(\pi/2)]\}^{1/8}$, where x_1 is the range with the potential equal to 0 and $x_a=32$ a.u. the range in which the absorbing potential is used. In three dimensions, the absorbing potential along the z direction is the same as that in one dimension. The same absorbing potential is used for the other, or ρ, direction, but with the range equal to 8 a.u.

A. Energies and transition moments in one dimension

The linear two-electron triatomic molecule $H_3{}^+$ has different symmetries in various states: The ground state is a singlet $X^1\Sigma_g^+$ and the first excited state with ungerade symmetry is also a singlet $B^1\Sigma_u^+$, as in H_2 [17]. The second excited state that can interact with the above two states is $E^1\Sigma_g^+$. All spatial symmetric functions satisfy the relation $\psi(x_1,x_2)=\psi(x_2,x_1)$ initially $(t=0)$. The initial wave function of the states is generated by propagating the field-free TDSE (see Ref. [17]) in imaginary time until convergence. The three-dimensional contour map of the wave functions for the ground state $X^1\Sigma_g^+$ of H_3^+ at the total internuclear distance between the two outer hydrogen atoms $R=10$ a.u. is given in Fig. 1(a) and that of the nonsymmetric case $H_3{}^+(n)$ is given in Fig. 1(b) for later discussion. The eigenvalues of these field-free states can be calculated from the wave functions using two methods. The first method proceeds by calculating the correlation function after propagating forward in time (without the laser field) and then using a Fourier transform with a window function [30]. The second method is to calculate directly the energy from the time-independent Schrödinger equation $H\Psi=E\Psi$ from the propagated initial wave function. The two methods give comparable results up to three decimal points. The energies of these states for internuclear distance R from 2.0 to 20 a.u. are given in Figs. 2(a) and 2(b). It can be seen from Figs. 2(a) and 2(b) that the 1D linear triatomic molecules $H_3{}^+$ and $H_3{}^+(n)$ (n means nonsymmetric, in which the short bond is fixed at 2.0 a.u.) are stable, with an equilibrium at $R_e\simeq 2.5$ a.u. Three-dimensional *ab initio* calculations give an equilibrium $R_e=$ 1.5112 a.u. for linear geometry. Our longer bond lengths are due to the softened Coulomb potential with $c=1$ in Eq. (1). Using small c would reduce R_e, but would lead to very high ionization rates. Thus a compromise has been made to use $c=1$ to be closer to the 3D ionization rates. The one-electron $H_3{}^{2+}$ potentials are similar to the two-electron $H_3{}^+$ system and are therefore not reported. At large R (>7 a.u.), the first three states become degenerate for both $H_3{}^{2+}$ and $H_3{}^+$ and from Fig. 2(a) $H_3{}^+$ dissociates to 2H + H^+ since the ionization potential of 1D H with $c=1$ is 0.67 a.u., whereas $H_3{}^{2+}$ goes to H + $2H^+$. However, for the nonsymmetric case, these states separate at larger internuclear distance, as shown in Fig. 2(b). The energy of the ground state for $H_3{}^{2+}(n)$ asymptotically goes to that of $H_2{}^+$+H, whereas for $H_3{}^+(n)$ it approaches that of H_2+H^+ and H + $H_2{}^+$ at large R.

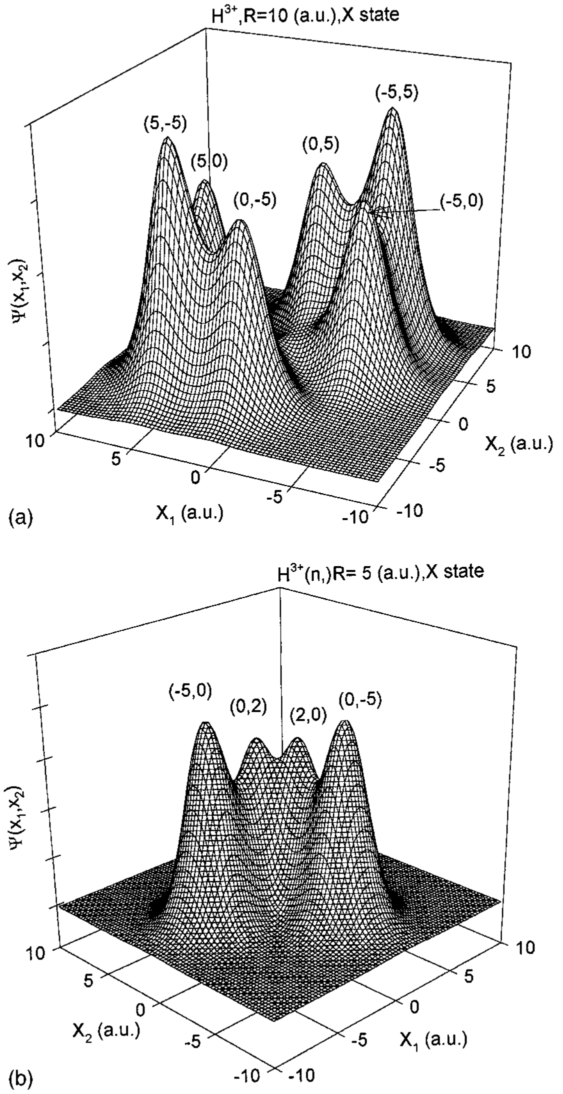

FIG. 1. Initial electron pair functions $\psi(x_1,x_2)$ for (a) the symmetric $H_3{}^+$, $X^1\Sigma_g^+$ state, $R_1=R_2=R/2=5$ a.u., and (b) the nonsymmetric $H_3{}^+(n)$, $X^1\Sigma$ state, $R_1=2$ a.u., $R_2=R=5$ a.u.

The first electronic transition moments μ for the two-electron symmetric $H_3{}^+$ and nonsymmetric $H_3{}^+(n)$ molecules are defined as $\mu=\langle\Psi_i(x_1,x_2)|x_1+x_2|\Psi_j(x_1,x_2)\rangle$ and are shown in Fig. 3(b). For $H_3{}^+$, the first transition moment μ_{12} (a), corresponding to the $X^1\Sigma_g^+\rightarrow B^1\Sigma_u^+$ transition, varies nearly linearly with R for large distances. The second transition $\mu_{23}(R)$ (b), corresponding to $B^1\Sigma_u^+\rightarrow E^1\Sigma_g^+$, shows similar linear behavior asymptotically. We show for comparison (c) the $H_2{}^+$ transition moment, which behaves as $R/2$ and is typical of charge resonance (CR) transitions [1,2,12,13,32]. Thus, in $H_2{}^+$, such $R/2$ behavior for

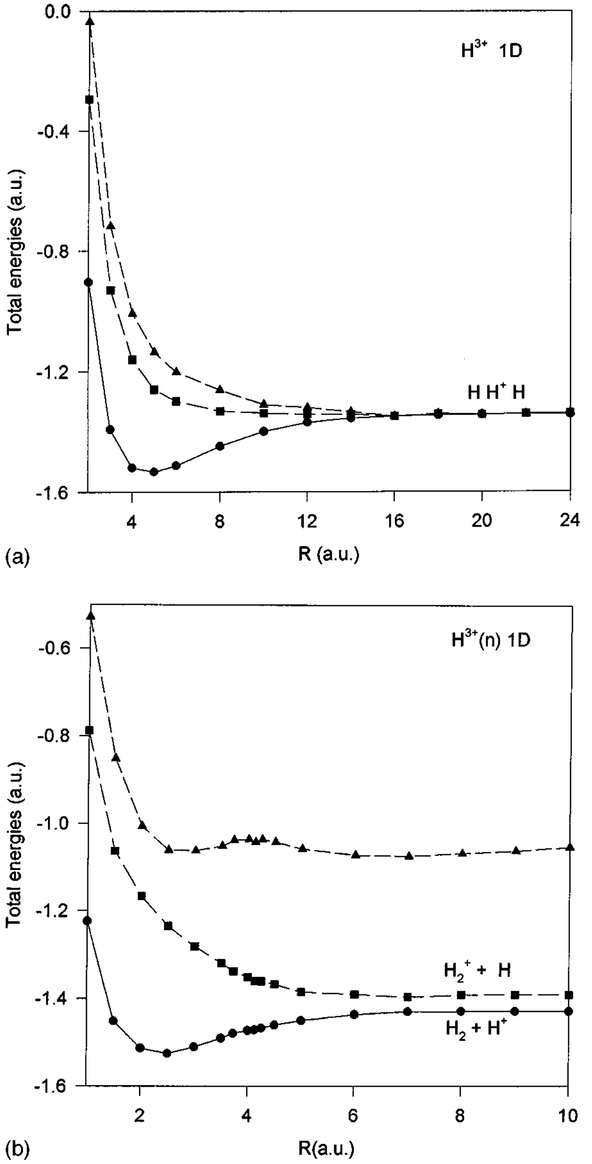

FIG. 2. Energies (one dimension, a.u.) for (a) H_3^+ and (b) $H_3^+(n)$.

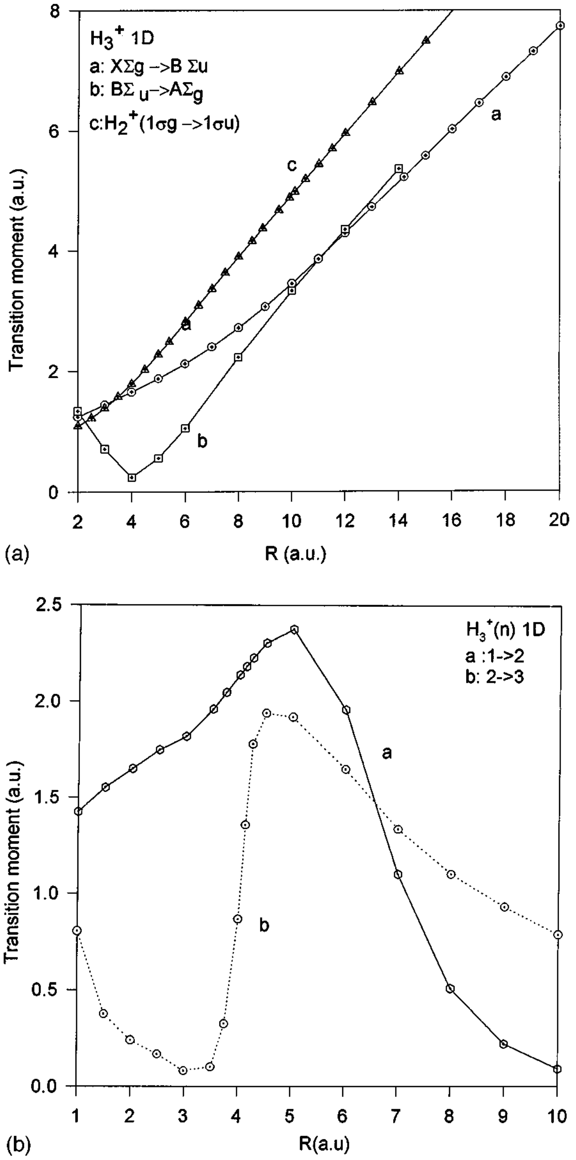

FIG. 3. Electronic transition moments μ (a.u.) for (a) H_3^+ and (b) $H_3^+(n)$.

the transition moment comes from the asymptotic form of the $1\sigma_g$ and $1\sigma_u$ molecular orbitals, $(1/\sqrt{2})[(1s_1) \pm (1s_2)]$, where $\mu_{12} = \langle 1\sigma_g | x | 1\sigma_u \rangle$. In H_3^{2+} and H_3^+, the $1\sigma_g \rightarrow 1\sigma_u \rightarrow 2\sigma_g$ transition moment can be shown to behave as $R/2\sqrt{2} \simeq 0.4R$ since the g orbitals are asymptotically $(1/\sqrt{2})((1s_2) \pm \{(1/\sqrt{2})[(1s_1)+(1s_3)]\})$ and the μ orbital is $(1/\sqrt{2})[(1s_1)-(1s_3)]$, where $(1s_i)$ is the $1s$ atomic orbitals or proton i [33]. Figure 3(a) shows clearly the CR character of both the first (a) and second (b) transitions in H_3^+, i.e., the electron is being transferred from one end of the molecule to the other by the laser field, with a moment close to the theoretical $0.4R$ value. As shown previously for H_2^+, it is the CR effect that creates divergent transition moments and hence large nonperturbative couplings with radiation fields with unusual effects such as laser-induced localization and large even-order harmonic generation [12,13]. In the case of the one electron, H_3^{2+}, a transition occurs around $R = 4.5$ a.u. from the $0.4R$ triatomic behavior to the $R/2$ diatomic behavior for the second $1\sigma_u \rightarrow 2\sigma_g$ transition, whereas the first $1\sigma_g \rightarrow 1\sigma_u$ transition decreases slowly to zero asymptotically. Thus, in the two-electron H_3^+ case, electron correlation maintains the CR effect for both transitions, whereas in the H_3^{2+} case, this effect diminishes asymptotically in the first transition. This reflects the different dissociation products of both molecules: $H_3^{2+} \rightarrow H^+ + H + H^+$, whereas $H_3^+ \rightarrow H + H^+ + H$. Clearly in the latter the CR transfer occurs over the whole length of the molecule at all times.

For the nonsymmetric $H_3^+(n)$ system, the near degeneracy of the dissociation products $H_2 + H^+$ and $H + H_2^+$ creates a CR-like first transition moment (a) with $R/2$ behavior [Fig. 3(b)]. Both first (a) and second (b) transition moments undergo a sharp decrease around $R = 5$ a.u. A similar behavior is found in $H_3^{2+}(n)$, the one-electron nonsymmetric case where the first transition moment μ_{12} is constant, that of H_2^+, in view of the dissociation product $H_2^+ + H^+$. The second transition moment $\mu_{23}(R)$ behaves initially as a CT

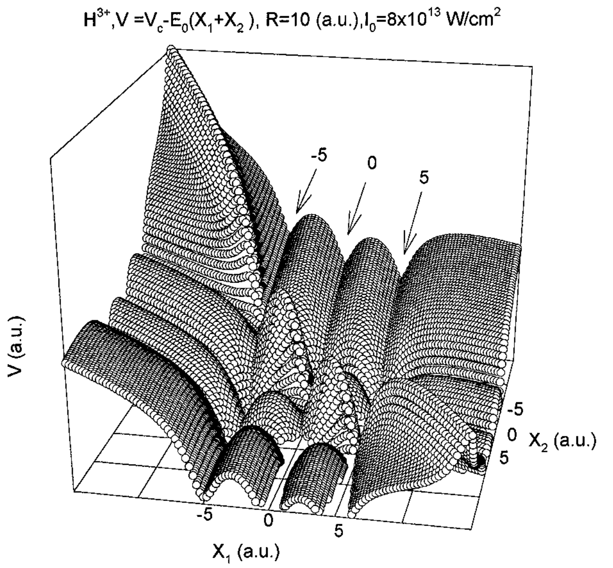

FIG. 4. Total static potential (V_c [Eq. (2)] $+V_{ext}$ [Eq. (1)]) at $R=10$ a.u. for 1D $H_3{}^+$; $E_0=2.5\times10^8$ V/cm and x_1 and x_2 are electronic coordinates.

$R/2$-like moment with a maximum at $R\simeq6$ a.u. We interpret this abrupt change of moment around $R\simeq5-6$ a.u. as a transition from delocalized (molecular orbitals) electrons at small R to a more localized region at large R in both one-electron $H_3{}^{2+}(n)$ and two-electron $H_3{}^+(n)$ systems. A similar behavior is found in the $X^1\Sigma_g^+\rightarrow B^1\Sigma_u^+$ transition of H_2 [17].

B. Ionization rates

The initial two-electron wave function for the symmetric $H_3{}^+$ and nonsymmetric $H_3{}^+(n)$ are illustrated in Figs. 1(a) and 1(b), respectively. In the symmetric case [Fig. 1(a)], one sees six peaks corresponding to the large resonance $H-H^+-H$ at electron position $(x_1,x_2)=(5,-5)$ and $(-5,5)$, the resonance $H-H-H^+$ at $(-5,0)$ and $(0,-5)$, and the resonance H^+-H-H at (0,5) and (5,0). The nonsymmetric case $H_3{}^+(n)$ [Fig. 1(b)] shows two major peaks at $(-5,2)$ and $(2,-5)$ corresponding to the charge resonance $H\leftrightarrow H^+\leftrightarrow H$ where $R=5$ a.u. is the largest neighbor proton-proton distance and $R_e=2$ a.u. is the equilibrium $H_2{}^+$ distance. The smaller peaks occuring at (0,2) and (2,0) correspond to the H^++H_2 resonance. An instantaneous electric field will tilt the Coulomb potential V_c [Eq. (2)] in the field direction. This is illustrated for the symmetric case, $H_3{}^+$ in Fig. 4, at a field intensity $I=8\times10^{13}$ W/cm^2 or, equivalently, $E_0=2.5\times10^8$ V/cm. The ridge along the diagonal $x_1=x_2$ represents the electron repulsion barrier, whereas the triple wells are the one-electron–proton binding potentials. Figure 1(a) shows clearly the three charge resonances for the pair of electrons bound in each well and separated by the repulsive ridge in the initial field-free ground state. In the presence of the instantaneous field E_0 Fig. 4 each electron can tunnel out from the high (negative x) potential region to the low (positive x) region.

The ionization rates in the presence of the time-dependent field $E_0(t)\cos(\omega t)$ is obtained by propagating in real time, the exact TDSE (1), using split-operator methods [31,32], with the initial wave functions illustrated in Fig. 1. The total rates Γ (s^{-1}) are calculated from the logarithmic decrease of the total probability or norm $N(t)$,

$$\ln N(t)=-\Gamma t,\quad N(t)=\int|\Psi(x_1,x_2,t)|^2dx_1dx_2. \quad (3)$$

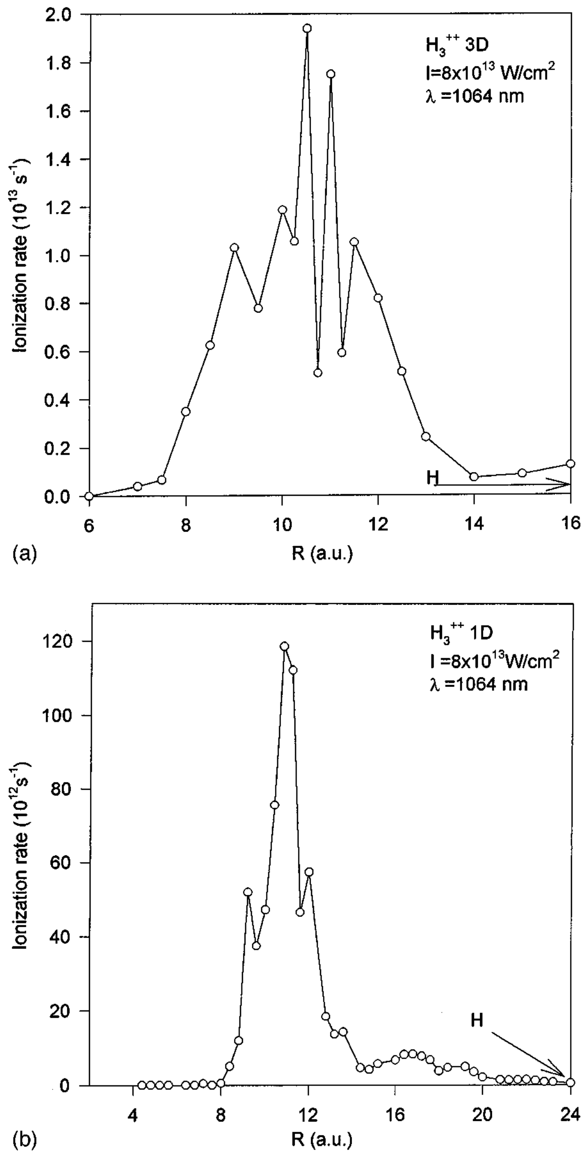

FIG. 5. Electronic ionization rates (s^{-1}) at $I=8\times10^{13}$ W/cm^2 and λ = 1064 nm for (a) 3D $H_3{}^{2+}$ and (b) 1D $H_3{}^{2+}$.

Several examples of calculated ionization rates are illustrated in Figs. 5 and 6. Thus, in Figs. 5(a) and 5(b) we compare an exact 3D calculation for $H_3{}^{2+}$ vs the 1D result for $H_3{}^{2+}$ with the softened ($c=1$) Coulomb potential in Eq. (1). The general forms of the ionization rate vs R for $I=8\times10^{13}$ W/cm^2, $\lambda=1064$ nm, and the same pulse envelope (five-cycle ramp) are similar in the exact 3D and model 1D cases. The principle feature to be underlined is the clear ionization enhancement that appears between 8 and 14 a.u. in both cases. A 20-fold increase of ionization occur for the 3D $H_3{}^{2+}$ case at the maximum ($R\simeq10.5$ a.u.) when compared to the asymptotic value corresponding to the H atom. In the

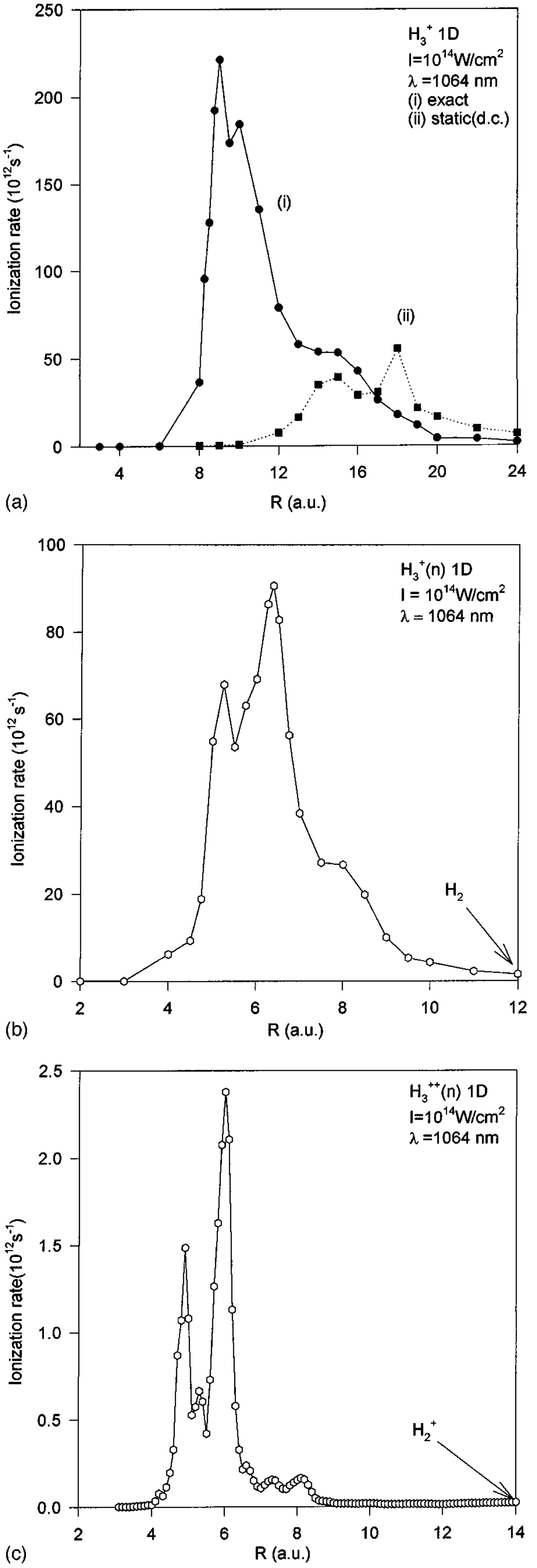

FIG. 6. Electronic ionization rates (s^{-1}) at $I=10^{14}$ W/cm^2 and λ = 1064 nm for (a) 1D $H_3{}^+$: (i) exact and (ii) static (dc) potentials; (b) 1D $H_3{}^+(n)$; and (c) 1D $H_3{}^{2+}(n)$.

1D case the increase is about 100-fold, i.e., the 1D model enhances the effect even further due to the lower dimensionality of electron trajectories.

This same enhancement of ionization is obtained for both the symmetric $H_3{}^+$ [Fig. 6(a)], and nonsymmetric $H_3{}^+(n)$ [Fig. 6(b)] 1D electron systems. (We add in Fig. 6(c) the one-electron $H_3{}^{2+}(n)$ nonsymmetric case for comparison with the two-electron case [Fig. 6(c)]. In the two-electron case, the enhanced ionization now occurs over a broader larger-R range, i.e., $8\leq R\leq 20$ when compared with the one-electron case [Figs. 5(b) and 6(c)]. We turn next to the physical interpretation of these enhanced ionization results.

III. ONE-ELECTRON IONIZATION

The lower-frequency region such as $\omega=0.0428$ a.u. or, equivalently, $\lambda=1064$ nm shows signatures of CREI in diatomic ions via laser-induced localization [12,13] and field-induced barrier suppression [5–7,13–16,20,21]. The latter quasistatic picture has been very useful in explaining high-intensity low-frequency atomic ionization as a field-induced tunneling phenomenon [34]. In the triatomic one-electron molecular ion case, the correlation of enhanced ionizations with a similar field-induced barrier tunneling model has been successful for the 3D nonsymmetric $H_3{}^{2+}$ molecule [18] and highly charged one-electron 1D triatomic molecules [22]. We examine below in detail the TDSE ionization results for the 3D symmetric case $H_3{}^{2+}$ as shown in Fig. 5(a). As seen in Fig. 4, in the presence of an instantaneous static field E_0, the total electron-proton potentials are tilted down at large electron nuclear position x. Along each coordinate x_1 or x_2, three barriers are prominent, which an ionizing electron encounters on its way out to large x.

As an example we show in Fig. 7(a) for the one-electron 3D symmetric $H_3{}^{2+}$ such a field distorted potential profile along the internuclear axis. We label V_1, V_2, V_3 as the barrier maxima that develop at 4, -4, and -12 a.u., at intensity 8×10^{13} W/cm^2 ($E_0=2.5\times10^8$ V/cm) for the total internuclear distance $R=14$ a.u. (or 7 a.u. between each proton). We give also the corresponding position of the first three static field levels E_1, E_2, E_3 as a function R. The latter are obtained as static field resonances in a TDSE calculation with constant static field (dc field) [12]. Crossing of the levels E_i with V_i's implies field-induced trapping of these levels with concomitant ionization suppression. Figure 7(b) shows that below $R=7$ a.u., all levels E_i, which at zero field are $1\sigma_g$, $1\sigma_u$, and $2\sigma_g$ levels, are above V_2 and V_3. All levels E_i are below V_1, the left outer barrier below $R=7$ a.u., in agreement with the rapid decline of ionization rates below this internuclear distance as illustrated in Fig. 5(a). Enhanced ionization begins to occur above $R=7$ a.u. up to $R=12$, where after a new sharp decline in ionization occurs. This can be rationalized from Fig. 7(b) as due to the complete trapping of levels E_2 and E_3 around $R=12$ by V_1 and V_2, respectively. Thus, as shown in Fig. 7(a), levels E_2 and E_3 are trapped by barriers V_2 and V_3 at $R=14$ a.u. and level E_2 will be subsequently trapped again beyond $R=14$ a.u. by V_2. Figure 7(a) thus provides a strong correlation between the enhanced ionization window $7\leq R\leq 14$ a.u. and the static above-barrier ionization model. A sharp maxima occurs around 10 and 11 a.u. as E_2 begins to tunnel appreciably

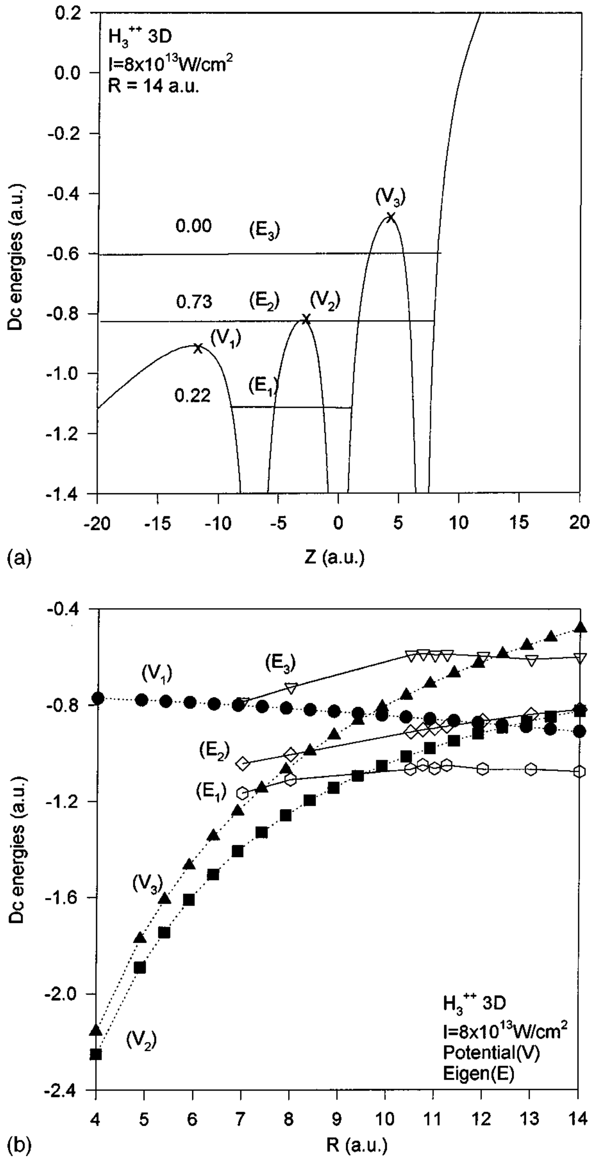

FIG. 7. Total static potential V_c+V_{ext} along the internuclear axis for linear 3D $H_3{}^{2+}$ at $I=8\times10^{13}$ W/cm^2 ($E=2.5\times10^8$ V/cm, for (a) $R=14$ a.u., with V_1,V_2,V_3 the barrier maxima, E_1,E_2,E_3 the static field levels, and their population after 20 cycles; and (b) V_1,V_2,V_3,E_1,E_2,E_3 as functions of R.

across the decreasing V_1 barrier. This sudden enhancement can be also correlated to CREI [12,13] as a laser-induced electron ionization. For a two-level system, the energy separation $\omega_{12}^0=\omega_2-\omega_1$ is renormalized by the time-dependent field such that [13,35,36].

$$\omega_{12}=\omega_{12}^0\, J_0(2\Omega_R/\omega), \tag{4}$$

where ω_{12}^0 is the field free-energy separation due to electron tunneling between the proton and Ω_R the Rabi frequency [$=eE\mu(R)$].

In the present case, the $1\sigma_g \rightarrow 1\sigma_u$ transition moment is clearly approximated by $\mu=R/2\sqrt{2}$ [see Fig. 3(a)] as discussed in Sec. II A. Zeros of $J_0(2\Omega_R/\omega)$ occur at 5.5 and 8.65 or, alternatively, at $R=7$ and 10.7 a.u. At such zeros, one expects tunneling suppression of the electron between the protons by the laser field since $\Delta\omega=0$ [12,13]. The field therefore induces tunneling ionization across the static barrier V_i and simultaneously suppresses tunneling between the Coulomb potential wells that competes with the ionization [13].

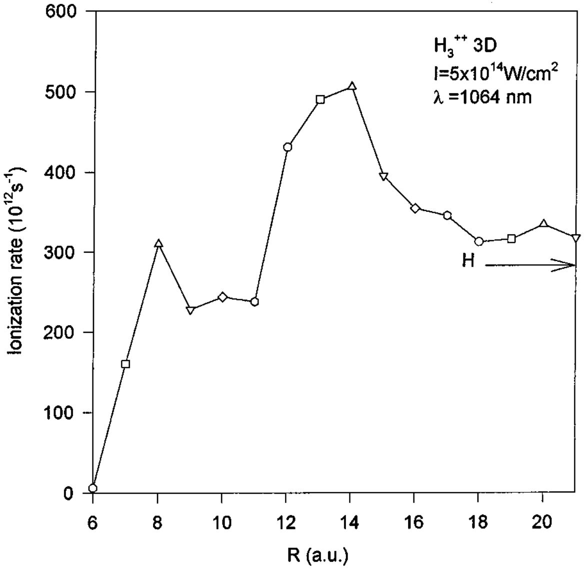

FIG. 8. Electronic ionization rates (s^{-1}) for 3D $H_3{}^{2+}$ at $I=5\times10^{14}$ W/cm^2 and $\lambda=1064$ nm.

The quasistatic field tunneling ionization interpretation becomes more valid for low laser frequencies and/or higher intensities. The latter is corroborated by Fig. 8, where we present the ionization rates for 3D $H_3{}^{2+}$ for the higher intensity 5×10^{14} W/cm^2 and the wavelength $\lambda=1064$ nm. Again there is a sharp rise in ionization rate around $R=8$ a.u., which approaches asymptotically the 3D H atom value. Thus again $H_3{}^{2+}$, where one electron is bound by three protons, has ionization rates comparable to and above that of the H atom for the same excitation conditions. The sharp peak at $R=8$ a.u. correlates strongly with the liberation of the lowest level ($1\sigma_g$ at zero field) at that distance in the presence of an equivalent static field [Fig. 9(a)]. The subsequent fall in ionization rate at $R=9$ a.u. seems to be due to the crossing of V_1 and V_2 at $R=8$ [Fig. 9(b)] such that at $R=9$ a.u. E_1 is trapped by the middle barrier V_2. Above $R=9$ it is the E_2 and E_3 levels that contribute free (above-barrier) ionization, whereas E_1 ionizes through tunneling as a H atom.

We conclude from the TDSE calculation for symmetric $H_3{}^{2+}$ that the enhanced ionization window $8\leqslant R\leqslant14$ a.u. obtained in the exact 3D simulation [Fig. 5(a)] and the model 1D case [Fig. 5(b)] can be correlated with a field-induced quasistatic above-barrier ionization, whereas the sharp peak at $R\simeq10$–11 a.u. can be rationalized in terms of field-induced localization and possibly also frequency resonance effects.

IV. TWO-ELECTRON IONIZATION

Previous time-dependent 1D calculations for two-electron atomic systems [32–38] have examined the role of correlation and provided insight into atomic one-electron versus two-electron photoionization. A previous 1D model of H_2

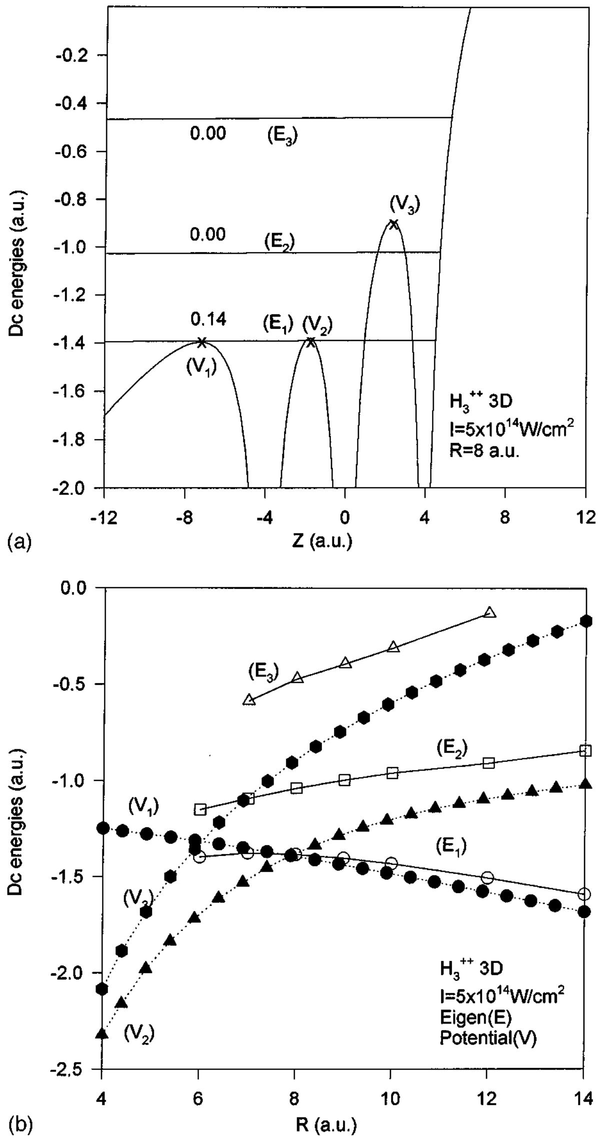

FIG. 9. Energy levels E and static potentials along the internuclear axis for 3D H_3^{2+} at $I=5\times10^{14}$ W/cm^2 for (a) $R=8$ a.u. and their population after 20 cycles and (b) as a function of R.

examined the high-frequency and high-intensity behavior of this molecule in the space transition representation [39] in which we already showed stabilization of the one-electron H_3^{2+} [28,29]. We examine here the symmetric H_3^+ and nonsymmetric $H_3^+(n)$ two-electron 1D systems using the same methods as we used previously for H_2 at intensities $I \geqslant 10^{14}$ W/cm^2 and $\lambda=$ 1064 nm [17].

The ionization rates for the symmetric and nonsymmetric linear molecule H_3^+ are illustrated in Fig. 6. Comparing with the single-electron case H_3^{2+} [Figs. 5(b) and 5(c)], one observes now a broader window for enhanced ionization. One main difference between the one-electron and two-electron molecular system can be deduced from the transition moments. Thus, in Fig. 3(a), we observe that the two successive moments $\mu_{12}(R)$ (a) and $\mu_{23}(R)$ (b) behave asymptotically as two equal CR transitions with moment near $0.4R$, the molecular orbital prediction discussed in Sec. II A. For the one-electron H_3^{2+}, the first moment $\mu_{12}(R)$ decreases for large R as the molecule dissociates to $H^+ + H^+ + H$. The second moment (c) is the CR moment with asymptotic value $R/2$ for H_2^+. Thus, in the two-electron case, two equal CR transitions dominate the photophysics as opposed to only one CR transition in the one-electron case. Further support for this hypothesis is obtained by examining the static field ionization rate (ii) illustrated in Fig. 6(a). Curve (ii) is obtained by ramping the field under the same condition as (i), but with a static field $E_0=(8\pi I_0/c)^{1/2}$, where I_0 is the peak intensity in the full time-dependent calculation (i). Thus, in the static field case, enhanced ionization occurs at large $R \simeq 12-20$ a.u., in the region where one-barrier ionization of level E_2 begins (see Fig. 7). Hence the shoulder around $R \simeq 14$ a.u. can be ascribed to the population of level E_2 for which a large CR transition moment occurs. Static field rate calculations for the one-electron case H_3^{2+} show this shoulder to be negligible, in agreement with its absence in Fig. 5(b) and the fact that the transition moment μ_{12} is weak in the one-electron case, but is a large CR moment for the second transition. Our conlusion is that electron correlation that keeps electrons apart enhances CR transition moments in the two-electron case, thus enhancing population of upper states more easily than in the one-electron case. The sharp onset of ionization in the one- and two-electron cases around $R \simeq 8$ a.u. correlates well with the above-barrier ionization of level E_3, which begins for $R \geqslant$ 7 a.u. in Fig. 7(b) due to the efficient population through the large CR moment μ_{23}: $R/2$ and $R/2\sqrt{2}$ for the one- and two-electron cases, respectively.

The nonsymmetric case, two-electron system $H_3^+(n)$, which dissociates into the two product channels $H_2 + H^+$ or $H_2^+ + H$ [see Fig. 2(b)], manifests two sharp peaks in the ionization rate as a function of R [Fig. 6(b)], the distance between the outer and inner protons (the H_2 distance remains fixed at $R=2$ a.u.). The same two peaks, albeit sharper, occur in the one-electron case $H_3^{2+}(n)$ [Fig. 6(c)]. Thus enhanced ionization is expected to be prominent, for $4 \leqslant R \leqslant 10$ a.u. in the $H^+ + H_2$ collision and $4 \leqslant R \leqslant 7$ in the $H^+ + H_2^+$ collision, with maxima at $R=5$ a.u. and then 7 or 6 a.u. The first maximum at $R=5$ a.u. would seem to correlate with maxima in the transition moment μ_{12} and μ_{23} [Fig. 3(b)], indicating a transition from delocalized electrons for small R to localized electrons at large R. In fact, $\mu_{12} \simeq R/2$ up to $R=5$ a.u., typical of the CR transition between H_2^+ and H or H_2 and H^+. The single-electron case $H_3^{2+}(n)$ has a first transition moment $\mu_{12}(R)$ equal to that of H_2^+, whereas the second transition moment $\mu_{23}(R)$ behaves as a CR transition $H_2^+ + H^+ \rightarrow H_2^{2+} + H$ up to $R=7$ a.u. Static field calculations for the latter 3D problem [17] show that $R=5$ a.u. also corresponds to the onset of above-barrier ionization of the first level E_1. Thus the decline of ionization for large R is to be interpreted as a rise of the external barrier [Fig. 7(a)] as transition moments decrease with large R.

Two-electron effects have been shown earlier for H_2 to influence electron ionization distributions at high intensities [17]. In the present triatomic case, Fig. 4 gives an indication of how electrons would ionize in a quasistatic model, for instance, at the peak intensity. Each electron will tunnel along its own coordinate $x_{1(2)}$ from one well to the other and through the low external barrier V_1 [Fig. 7(a)]. This is the preferred scenario for the one-electron system H_3^{2+}. In the

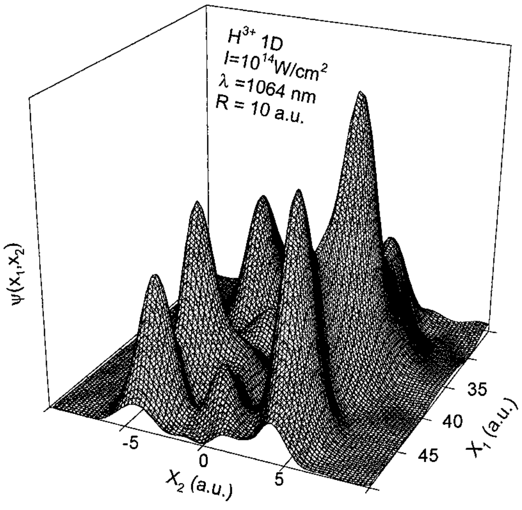

FIG. 10. Propagating electron pair wave packet $\psi(x_1,x_2,t)$ for 1D $H_3{}^+$ at $I=8\times10^{14}$, $\lambda=1064$ nm, $R=10$ a.u. and $t=20.75$ cycles (74 fs) at large x_1 and small x_2.

two-electron case, the electron pair function is quasilocalized in six wells [see Fig. 1(a)] with major peaks at positions $(x_1,x_2)=(5,-5)$ or $(-5,5)$, corresponding to the least repulsive electron resonance $H-H^+-H$. Thus either electron independently will ionize by following the Coulomb potential canal at $R=\pm5$ created by the second electron-proton attraction. This is clearly evident in Fig. 10, where we illustrate the electron pair function $\psi(x_1,x_2)$ for large x_1 along the x_2 canal at $R=\pm5$, after having propagated 20.75 cycles at $I=10^{14}$ W/cm^2, $\lambda=1064$ nm, and $R=10$ a.u. We see clearly propagation of electron 1 to large distances as it ionizes, whereas sharp peaks remain at $x_2=\pm5$, corresponding to localization of electron 2 at both ends of the molecule. We note that the peaks are largest at $R=+5$, corresponding to trapping of electron 2 in the right-hand lower well. We note the same numerical trapping of electron 2 at $R=0$, the middle well. Thus the quasistatic pictures [Figs. 4 and 7(a)] show clearly that the electron wave packet is indeed shaped by the static field induced barrier during the ionization process.

As in our H_2 work, we further explore the two-electron dynamics by partitioning the potential space (Fig. 4) into separate regions a,b,c,e as illustrated in the right-hand inset of Fig. 11(a). a is a box ±16 a.u., containing the initial $H_3{}^+$ [Fig. 1(a)]. We shall also compare it to a larger box d with dimension ±32 a.u. The total box e has dimension ±128 a.u. The four regions b correspond to the outgoing canals around $R=\pm5$ a.u., each with width 32 a.u. The outgoing flux in this region should correspond mainly to independent one-electron ionization as illustrated by Fig. 10. Finally, region c corresponds to the diagonals. The region $x_1=x_2$ is clearly forbidden by electron repulsion corresponding to the high ridge in Fig. 4, where the region $x_1=-x_2$ should be populated by two-electron effects.

Figures 11 and 12 illustrate the probabilities for each region as measured by the norm in each as a function of time. The decaying slopes for larger time give an estimate of these ionization rates in each region. The consistency of the method is verified by comparing rates Γ_a in the smaller a box (±16 a.u.) around the initial molecule with the rates Γ_d in the larger d box (±32 a.u.). In both low intensity (Fig. 11) $I=10^{14}$ W/cm^2 and $\lambda=1064$ nm and high intensity (Fig. 12) $I=10^{15}$ W/cm^2 and $\lambda=532$ nm, one observes identical Γ_a and Γ_d. We note that Γ_a, Γ_d, and Γ_e at $I=10^{14}$ W/cm^2, approach 0.5 probability at large time (10 cycles=36 fs), indicating that one electron remains. This can also be seen in Fig. 10, where the sharp peaks show trapping of the electrons. The ionizing electron is mainly in region b as the probability in region b quickly rises to 0.4 in 3 fs and then decays as the electron leaves the box. Figure 11 illustrates therefore single-electron ionization as being dominant at 10^{14} W/cm^2. Very little electron density appears in

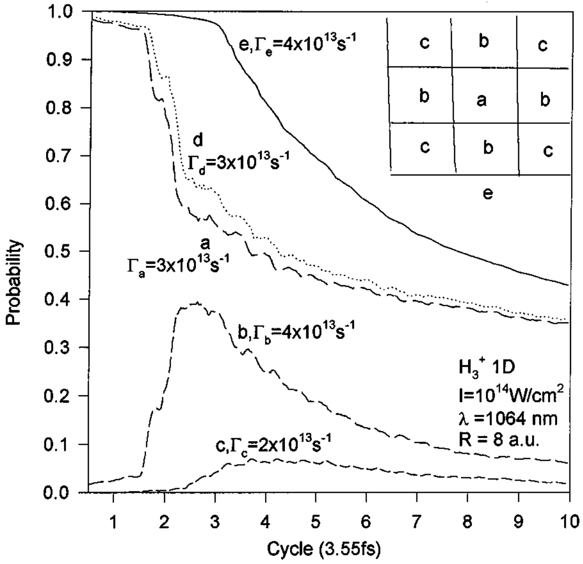

FIG. 11. Electron pair probabilities and ionization rates Γ (s^{-1}) for 1D $H_3{}^+$ at $I=10^{14}$ W/cm^2, $\lambda=1064$ nm, and $R=8$ a.u., for various regions a,b,c,d,e: $|a|\leq16$ a.u., $|d|\leq32$ a.u., and $|e|\leq256$ a.u.

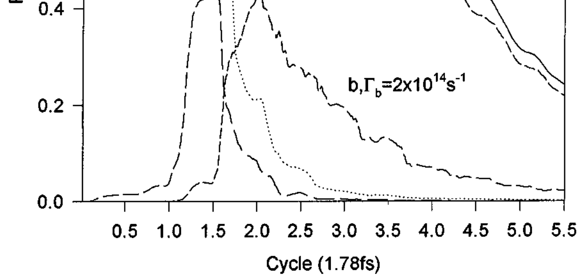

FIG. 12. Electron pair probabilities and ionization rates Γ (s^{-1}) for 1D $H_3{}^+$ at $I=10^{15}$ W/cm^2, $\lambda=532$ nm, and $R=8$ a.u., for various regions a,b,c,d,e: $|a|\leq16$ a.u., $|d|\leq32$ a.u., and $|e|\leq256$ a.u.

the two-electron region, region *c* ($<10\%$). Increasing the frequency ($\lambda = 532$ nm, $\omega = 0.0856$ a.u.) and increasing the intensity to 10^{15} W/cm^2 produces quite different results as illustrated in Fig. 12. The total ionization rate Γ_e has gone up by about one order of magnitude. The probability in the two-electron region *c* increases to about 75% in three cycles (6 fs), whereas the probability in the one-electron region increases to 55% in about two cycles (3.5 fs). The decay rates Γ_b, Γ_c, and Γ_e are nearly identical, suggesting that they represent the same physical phenomenon, i.e., one-electron ionization. The considerable presence of density in region *c*, the two-electron region where $x_2 = -x_1$, indicates the strong influence of electron repulsion in the ionization process. Whereas in region *b* the electrons ionize independently, in region *c* they do so under the influence of electron repulsion and thus ionize in different directions. Electron repulsion or correlation is thus seen to operate at later times, three cycles, whereas independent electron ionization occurs at earlier times, two cycles.

ACKNOWLEDGMENTS

We thank the Natural Sciences and Engineering Research Council of Canada for support of the present research. All calculations were performed on the IBM-SP2 parallel computer of the Centre d'Application en Calcul Parallèle de l'Université de Sherbrooke.

---

[1] *Atoms in Intense Laser Fields*, edited by M. Gavrila (Academic, San Diego, 1992).
[2] A. D. Bandrauk *Molecules in Laser Fields* (Marcel (Dekker, New York, 1993), Chaps. 1 and 3.
[3] A. D. Bandrauk, E. Aubanel, and J. M. Gauthier, Laser Phys. **3**, 381 (1993).
[4] A. Giusti-Suzor, F. H. Mies, L. F. Dimauro, E. Charron, and B. Yong, J. Phys. B **28**, 309 (1995).
[5] K. Codling, L. J. Frasinski, and P. A. Heatherly, J. Phys. B **22**, 1321 (1989).
[6] L. J. Frasinski, M. Stankiewiez, P. A. Hatherly, G. M. Cross, K. Codling, A. J. Langley, and W. Shaikh, Phys. Rev. A **46**, R6789 (1992).
[7] J. H. Posthumus, L. J. Frasinski, A. J. Giles, K. Codling, J. Phys. B **28**, L349 (1995).
[8] M. Schmidt, D. Normand, and C. Cornaggia, Phys. Rev. A **50**, 5037 (1994).
[9] C. Cornaggia and M. Schmidt, J. Phys. B **27**, L123 (1994).
[10] D. Normand and M. Schmidt, Phys. Rev. A **53**, R1958 (1996).
[11] S. Chelkowski, T. Zuo, and A. D. Bandrauk, Phys. Rev. A **46**, R5342 (1992).
[12] T. Zuo, S. Chelkowski, and A. D. Bandrauk, Phys. Rev. A **48**, 3837 (1993).
[13] T. Zuo, S. Chelkowski, and A. D. Bandrauk, Phys. Rev. A **53**, R2571 (1995).
[14] S. Chelkowski and A. D. Bandrauk, J. Phys. B **28**, L723 (1995).
[15] S. Chelkowski, T. Zuo, O. Atabek, and A. D. Bandrauk, Phys. Rev. A **52**, 2977 (1995).
[16] S. Chelkowski, A. Conjusteau, T. Zuo, and A. D. Bandrauk, Phys. Rev. A **54**, 3235 (1996).
[17] H. Yu, T. Zuo, and A. D. Bandrauk, Phys. Rev. A **54**, 3290 (1996).
[18] T. Zuo and A. D. Bandrauk, Phys. Rev. A **54**, 3254 (1996).
[19] T. Zuo, A. D. Bandrauk, and P. B. Corkum, Chem. Phys. Lett. **259**, 313 (1996).
[20] T. Seideman, M. Y. Ivanov, and P. B. Corkum, Phys. Rev. Lett. **75**, 2819 (1995).
[21] M. Y. Ivanov, T. Seideman, P. B. Corkum, F. Ilkov, and P. Dietrich, Phys. Rev. A **54**, 1541 (1996).
[22] T. Seideman, M. Y. Ivanov, and P. B. Corkum, Chem. Phys. Lett. **252**, 181 (1996).
[23] E. Constant, H. Stapelfeld, and P. B. Corkum, Phys. Rev. Lett. **76**, 4140 (1996).
[24] M. Plummer, J. F. McCann, J. Phys. B **29**, 4625 (1996).
[25] J. H. Posthumus, M. R. Tomson, A. J. Giles, and K. Codling, Phys. Rev. A **54**, 905 (1996).
[26] M. B. Boik, M. Pont, and R. Shakeshaft, Phys. Rev. A **54**, 570 (1996).
[27] K. C. Kulander, F. H. Mies, and K. J. Schafer, Phys. Rev. A **53**, 2562 (1996).
[28] J. Tennyson, Rep. Prog. Phys. **57**, 421 (1995).
[29] T. Zuo and A. D. Bandrauk, Phys. Rev. A **51**, R26 (1995).
[30] M. O. Feit, J. A. Fleck, and A. Steigt, J. Comput. Phys. **47**, 412 (1982).
[31] A. D. Bandrauk and H. Shen, J. Chem. Phys. **99**, 1185 (1993).
[32] R. S. Mulliken, J. Chem. Phys. **7**, 20 (1939).
[33] P. W. Atkins, *Molecular Quantum Mechanics* (Oxford, London, 1985).
[34] P. B. Corkum, N. H. Burnett, and F. Brunel, Phys. Rev. Lett. **62**, 1259 (1989).
[35] C. Cohen-Tannoudji, J. Dupont-Roc, and G. Grynstein, *Atom-Photon Interactions* (Wiley, New York, 1992), p. 407.
[36] M. Y. Ivanov, P. B. Corkum, and P. Dietrich, Laser Phys. **3**, 375 (1993).
[37] R. Grobe and J. H. Etherly, Phys. Rev. Lett. **68**, 290 (1992).
[38] S. L. Haan, R. Grobe, and J. H. Etherly, Phys. Rev. A **50**, 378 (1994).
[39] H. Wiedemann and J. Mostowski, Phys. Rev. A **49**, 2719 (1994).